2021 43rd Annual International Conference of the
IEEE Engineering in Medicine & Biology Society (EMBC)
Oct 31 - Nov 4, 2021. Virtual Conference

Plantarflexion Moment Prediction during the Walking Stance Phase with an sEMG-Ultrasound Imaging-Driven Model

Qiang Zhang, Natalie Fragnito, Alison Myers, and Nitin Sharma*

***Abstract*—Many rehabilitative exoskeletons use non-invasive surface electromyography (sEMG) to measure human volitional intent. However, signals from adjacent muscle groups interfere with sEMG measurements. Further, the inability to measure sEMG signals from deeply located muscles may not accurately measure the volitional intent. In this work, we combined sEMG and ultrasound (US) imaging-derived signals to improve the prediction accuracy of voluntary ankle effort. We used a multivariate linear model (MLM) that combines sEMG and US signals for ankle joint net plantarflexion (PF) moment prediction during the walking stance phase. We hypothesized that the proposed sEMG-US imaging-driven MLM would result in more accurate net PF moment prediction than sEMG-driven and US imaging-driven MLMs. Synchronous measurements including reflective makers coordinates, ground reaction forces, sEMG signals of lateral/medial gastrocnemius (LGS/MGS), and soleus (SOL) muscles, and US imaging of LGS and SOL muscles were collected from five able-bodied participants walking on a treadmill at multiple speeds. The ankle joint net PF moment benchmark was calculated based on inverse dynamics, while the net PF moment prediction was determined by the sEMG-US imaging-driven, sEMG-driven, and US imaging-driven MLMs. The findings show that the sEMG-US imaging-driven MLM can significantly improve the prediction of net PF moment during the walking stance phase at multiple speeds. Potentially, the proposed sEMG-US imaging-driven MLM can be used as a superior joint motion intent model in advanced and intelligent control strategies for rehabilitative exoskeletons.**

I. Introduction

Human ankle plantar flexors generate a large burst of "push-off" mechanical power at the late stance phase, enabling the forward propulsion during walking movement. Due to neurological disorders or injuries like spinal cord injury, stroke, and multiple sclerosis, the weakened function or dysfunction of plantar flexors is likely to cause a dramatic decrease in the "push-off" power. Consequently, these mobility disorders considerably impair normal walking and cause poor energy economy [1]. Recent neurorehabilitation techniques to improve weakened ankle plantarflexion (PF) function primarily focus on utilizing powered ankle exoskeletons [2], [3], soft exosuits [4], and functional electrical stimulation (FES) [5]. To maximize the benefits of neurorehabilitation, patients must be actively involved in training procedures with the robotic devices. Effective assistance during patient training requires intuitive human-in-the-loop control strategies. One representative control strategy is known as assist-as-needed (AAN) control [6], which is dependent on the accurate determination of continuous human volitional motion intention, such as muscle contraction force or joint moment. Conventional human limb continuous intention detection is reliant upon the human-machine-interaction measurements from mechanical sensors, such as force or torque sensors. The mechanical sensors are typically installed on a rigid and bulky frame, which limits the system's wearability and increases susceptibility to measurement inaccuracies due to the misalignment of the bionic joint center and human joint center, introducing undesirable interaction forces [7].

In recent decades, non-invasive neuromuscular signals have been investigated to estimate continuous human limb volitional motion and motion intention. For example, by employing a Hill-type neuromuscular model-based or model-free (machine learning-type) calibration methods between sEMG signals and limb mechanical functions, e.g., joint moment [8], [9] and angular position [10], [11], human limb continuous movement intention can be estimated in a manner of forward dynamics. However, sEMG signals suffer from interference or cross-talk from adjacent muscles, and cannot measure the activity of deep layer muscles [12]. Alternatively, two-dimensional brightness mode (B-mode) ultrasound (US) imaging allows one to see the musculature of the targeted muscle *in vivo*, and is considered as another non-invasive neuromuscular signal that could mitigate the shortcomings caused by using sEMG. In the literature, the most frequently used architectural features from US images include pennation angle [13], fascicle length [14], [15], muscle thickness (MT) [16], [17], and cross-sectional area [18]. These features have been used to correlate with joint mechanical functions during isometric or isokinetic cases by using Hill neuromuscular model (HNM)-based or model-free approaches [9], [19], [20].

So far, the literature in this field has focused on employing uni-modal bio-signals, i.e., using either characteristics from sEMG signals or US signals for the continuous estimation of human limb volitional motion and intention. A recent review study [21] made a case of fusing multiple sensing technologies, known as multi-modal bio-signals, to improve the accuracy of human intention estimation or prediction.

Q. Zhang, N. Fragnito, A. Myers, and N. Sharma are with the UNC/NC State Joint Department of Biomedical Engineering, NC State University, Raleigh, NC 27695 USA (e-mail: qzhang25@ncsu.edu; njfragni@ncsu.edu; abmyers@ncsu.edu; nsharm23@ncsu.edu). (*Corresponding author: Nitin Sharma) This work was funded by NSF CAREER Award # 1750748.

Recent studies have shown the advantages of using dual-modal bio-signals (sEMG and US imaging) over uni-modal bio-signals (sEMG or US imaging) towards the volitional ankle moment prediction in cyclic isometric dorsiflexion task [9], cyclic isometric PF task [22], and dynamic cycling's PF task [19], based on either HNM or machine learning models. However, the superior performance of using dual-modal bio-signals during more complex functional tasks, like periodic walking, remains unexplored. Therefore, this study investigates a dual-modal approach, called sEMG-US imaging-driven multivariate linear model (MLM), to predict ankle joint net PF moment during the walking stance phase with the consideration of both sEMG- and US imaging-derived neuromuscular features from both lateral gastrocnemius (LGS) and soleus (SOL) muscles. It is hypothesized that by using the proposed MLM, the net PF moment prediction error will be significantly reduced compared to the sEMG-, and US imaging-driven MLMs.

II. Methods

A. Subjects

The study was approved by the Institutional Review Board (IRB) at North Carolina State University (IRB number: 20602). Five young participants (3M/2F, age: 25.4±3.1 years old, height: 1.77±0.10 m, weight: 78.0±21.1 kg) without any neuromuscular or orthopedic disorders within the last six months, were recruited in this study. The participants were familiarized with the procedures and they signed an informed consent form before participation.

B. Experimental Protocol, Data Collection and Processing

Figure 1 (a) summarizes the experimental setup for the participants to perform static anatomical poses and dynamic gait trials (walking speeds changing from 0.5 m/s to 1.5 m/s), and Fig. 1 (b) presents the workflow of the sEMG-US imaging-driven MLM in calibration and prediction procedures. During all trials, the three-dimensional coordinates of 39 retro-reflective markers positioned on the participant's lower extremities were recorded using a 12-camera motion capture system (Vicon Motion Systems Ltd, Los Angeles, CA, USA) at 100 Hz. During the dynamic gait trials, the GRF signals were collected at 1000 Hz synchronously by using in-ground force plates (AMTI, Watertown, MA, USA) mounted on an instrumented treadmill (Bertec Corp., Columbus, OH, USA). Both GRF signals and markers trajectories were low-pass filtered with a fourth-order Butterworth filter, and the cut-off frequencies (between 2 and 8 Hz) were determined according to the analysis in [23]. The markers trajectories and GRF signals from static poses and dynamic gait trials were used for joints kinematics and kinetics calculation in Visual 3D (C-Motion, Rockville, MD, USA).

During the dynamic gait trials, 4 wired sEMG sensors (SX230, Biometrics Ltd, Newport, UK) were attached to the shank skin through a double-sided tape to non-invasively record the electrical signals from TA, LGS, MGS, and SOL muscles at 1000 Hz synchronously through Nexus 2.9. sEMG signals were band-pass filtered to the bandwidth between 20 Hz and 450 Hz, and then full-wave rectified and low-pass filtered with a cut-off frequency of 6 Hz. A similar US transducer setup was applied in the walking experiments as described in [22]. The US radio frequency (RF) data were recorded at 1000 frames per second synchronously with markers trajectories, GRF, and sEMG signals by using a pulse sequence trigger signal generated from Nexus 2.9, and then were beamformed to get the B-mode US images as shown in Fig. 1 (b). A commercial US imaging processing toolbox *UltraTrack* [24] was applied to determine the temporal sequences of the LGS and SOL muscles' thickness based on the adaptive optical flow tracking algorithms. First, one region of interest that encompassed the LGS and SOL muscles was selected as the area between the superficial and deep aponeuroses. Then, 10 vertical lines were manually defined with evenly distributed distances in the LGS's region and SOL's region on the first US imaging frame, respectively, as shown in Fig. 1 (b). Key-frame correction [24] was applied to minimize the time-related drift of MT's cyclical pattern over the 20-second walking, where the key-frames were selected to be at heel-strike and toe-off time points. After each correction, the new key-frame's vertical lines positions were determined by applying an affine transformation to the key-frame before it. Finally, the temporal sequence of the mean value of those 10 vertical lines' length from LGS and SOL muscles were calculated for LGS's MT and SOL's MT, respectively. The MT signals of both LGS and SOL muscles were then low-pass filtered with a cut-off frequency of 4 Hz.

The objective of the model calibration was to minimize the error between the net PF benchmark (calculated by using Visual 3D based on the inverse dynamics (ID)) and the calibrated net PF moment from the MLM by adjusting unknown parameters of the MLM through the least-squares algorithm. Since human walking function results in highly nonlinear dynamics, currently, researchers in the biomechanics community believe the most accurate and efficient way to calculate the net moment of an individual joint is based on the ID, so we applied the ID-derived net moment as a benchmark for models calibration. For the MLM calibration with a single-speed mode, the ankle joint's kinematics, kinetics, sEMG signals, and US imaging data from randomly selected 10 stance phase cycles of a single speed were used. For the MLM calibration with an inter-speed mode, the 10 stance phase cycles were composed of 2 stable cycles from each of five walking speeds. By manually reducing the inclusion of input channels for the MLM, we could derive the corresponding sEMG-driven MLM and US imaging-driven MLM. Either the single-speed modes or inter-speed mode, each calibrated MLM together with new data sets from 2 stance phase cycles, that were not involved in the calibration procedures, were used for MLMs-based net PF moment prediction and evaluation under each speed.

For the evaluation of the prediction performance by using each type MLM, the root mean square error ($RMSE$) normalized to individual peak net PF moment ($N-RMSE$), $RMSE$ normalized to individual body weight (BW −

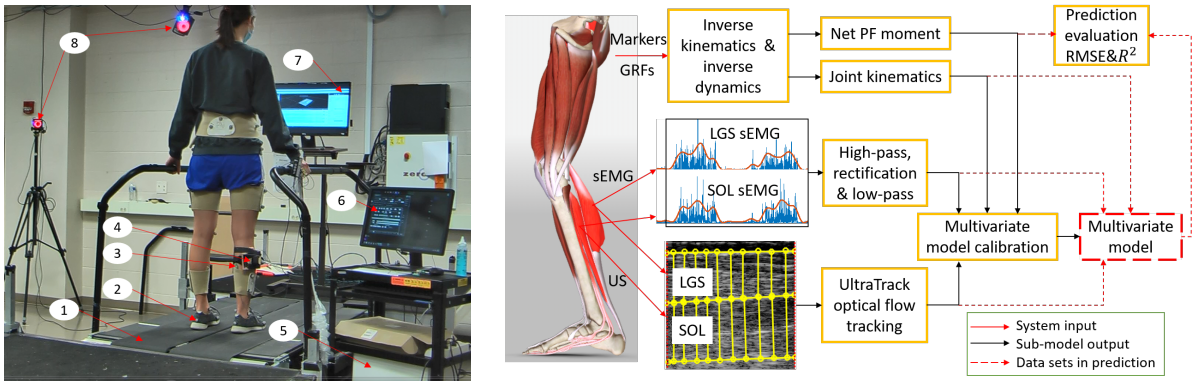

(a) (b)

Figure 1: (a) Illustration of walking experimental setup. (1) Instrumented treadmill with two split belts and in-ground force plates. (2) 39 retro-reflective markers on participant's lower body. (3) A single US transducer to image both LGS and SOL muscles. (4) Four sEMG sensors to record signals from LGS, MGS, SOL, and tibialis anterior (TA) muscles. (5) Ultrasound imaging machine to collect radio frequency (RF) data. (6) Computer screen to show B-mode ultrasound imaging. (7) Computer screen to show live markers and segment links of the participant. (8) 12 motion capture cameras. (b) Schematic illustration of the proposed sEMG-US imaging-driven MLM calibration and prediction workflow.

$RMSE$), and coefficient of determination (R^2) values, between the predicted net PF moment and ID-calculated net PF moment, were calculated and compared.

C. Statistical Analysis

Shapiro-Wilk parametric hypothesis test was used to determine the normality of the corresponding $N-RMSE$, $BW-RMSE$, and R^2 values of each prediction step by using the sEMG-/US imaging-/sEMG-US imaging-driven MLMs based on the single-speed modes calibration and inter-speed mode calibration. According to the results of the Shapiro-Wilk test, two-way repeated-measure analysis of variance (ANOVA) or Friedman's tests followed by a Tukey's honestly significant difference tests (Tukey's HSD) was applied to evaluate the effect of MLMs' category and walking speed on those three different evaluation criteria in the prediction with different walking scenarios. All p-values were adjusted using a Bonferroni correction for the Tukey's HSD, and the significant difference level was chosen as $p < 0.05$ for all statistical tests. Effect sizes were reported as η_p^2 and Cohen's d for main effects from ANOVA or Friedman's tests and pairwise comparisons from Tukey's HSD, respectively.

III. Results and Discussions

A. Ankle joint's kinematics and kinetics, plantar flexors' neuromuscular features during walking

Figure 2 (a) shows the mean and standard deviation (SD) of the right ankle joint angular position, velocity, and net moment changes across all normalized gait cycles within 20 seconds data collection at each walking speed on Sub01 (data from other participants are very similar), where 0% represents the instant heel-strike occurred. For this participant, there were approximately 12, 13, 15, 17, and 19 gait cycles during 20 seconds. Each gait cycle was segmented to the stance phase and swing phase with an indicator that the GRF's z-axis value was equal to 5% of the participant's BW. The walking experimental results on the treadmill from five participants show that the transition from the stance phase to the swing phase lies between 60% and 70% of the normalized gait cycle, as can be seen in Fig. 2 (a). Figure 2 (b) shows the processed neuromuscular features from US imaging and sEMG signals of LGS and SOL muscles during the stance phase at different walking speeds on Sub01. The upper two rows present the LGS and SOL MT changes, while the lower two rows present the muscle's low-pass filtered sEMG changes. By comparing the shadowed areas in Fig. 2 (b) of the same feature across speeds, we observed that features' deviations are higher at a slower speed, like 0.5 m/s, than at higher speeds. This implies that keeping a consistent gait pattern at a slower walking speed is more challenging than at a higher walking speed. Given the similar waveforms between each neuromuscular feature and net PF moment, we calculated and compared the correlation coefficients between sEMG and net PF moment, and between MT and net PF moment, as shown in Table I. We did not observe a significant difference in the correlation coefficients among the features ($p = 0.201$) or among the walking speed ($p = 0.112$), which indicated the MT and sEMG signals might have comparable capabilities to predict net PF moment at multiple speeds.

B. Net PF moment prediction performance based on MLMs

In this subsection, the continuous ankle joint net PF moment prediction results from the proposed sEMG-US imaging-driven MLM and baseline sEMG-driven/US imaging-driven MLMs are evaluated and compared. Fig. 3 shows the prediction results with the single-speed mode and inter-speed mode calibration MLMs in a representative

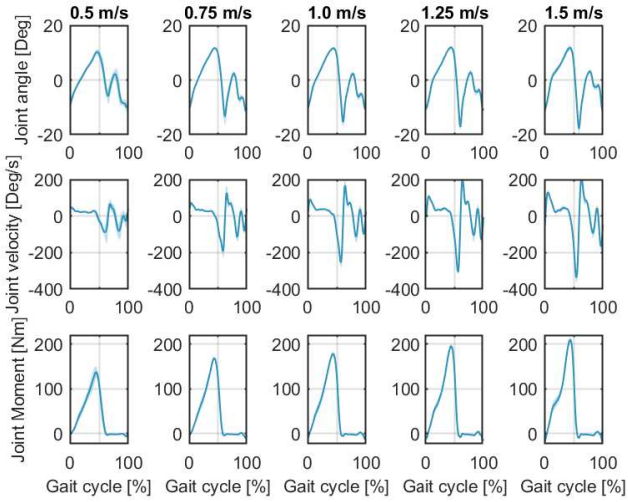

(a) Ankle joint kinematics and kinetics during normalized gait cycle

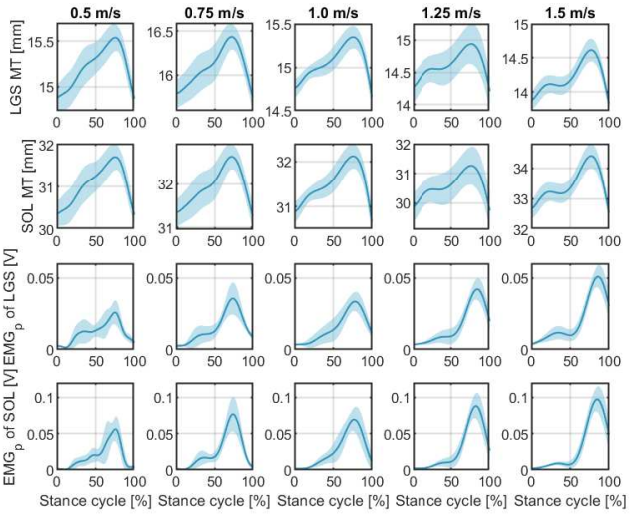

(b) Neuromuscular measurements from plantar flexors during normalized stance cycle

Figure 2: Right ankle joint kinematics and kinetics data, and plantar flexors' neuromuscular measurements during walking stance phase at different walking speeds on Sub01. The solid lines report the mean value of each variable across all gait cycles during the 20 seconds at each speed, and the light shadows report the standard deviation of each variable.

walking trial at 1.0 m/s on Sub05. In Fig. 3, with the single-speed mode calibration, the mean and SD values of the net PF moment prediction $RMSE$ are 14.71±0.69 Nm, 14.03±0.93 Nm, and 12.61±0.87 Nm with respective to the sEMG-, US imaging-, and sEMG-US imaging-driven MLMs, respectively. With the inter-speed mode calibration, the mean and SD values of the net PF moment prediction $RMSE$ are 16.79±0.81 Nm, 16.51±0.87 Nm, and 12.93±1.09 Nm, respectively. Overall, the individual prediction $RMSE$ values by using the sEMG-US imaging-driven MLM are lower than using the sEMG-driven and US imaging-driven MLMs for both single-speed mode and inter-speed mode. To compare the generic net PF moment prediction performance across participants, the mean and SD values of the prediction $BW-RMSE$, $N-RMSE$, and R^2 values across five participants are shown in Fig. 4. The subplots from (a) to (f) rectangular box in each row represent the applied calibrated MLMs were based on walking data with five single-speed modes and one inter-speed mode. In each rectangular box, like (a), the $x-$axis labels represent the prediction scenarios at five different speeds. From Fig. 4, we observed that $BW-RMSE$, $N-RMSE$, and R^2 values are minimized when the applied calibrated single-speed mode is close to the current prediction speed scenario, regardless of the applied MLM category. Furthermore, the calibrated inter-speed mode can effectively constrain the $BW-RMSE$, $N-RMSE$, and R^2 values to a small variation range among all prediction speed scenarios, regardless of the applied MLM category.

Shapiro-Wilk tests show that all $N-RMSE$, $BW-RMSE$, and R^2 values between the predicted and ID-calculated net PF moment by applying each MLM follow normal distribution. The results of two-way repeated-measure ANOVA show that $BW-RMSE$ values are significantly affected by the calibration speed mode (main effect, $p<0.001$, $\eta_p^2=0.162$) and applied MLM category (main effect, $p<0.001$, $\eta_p^2=0.082$), $N-RMSE$ values are significantly affected by the calibration speed mode (main effect, $p<0.001$, $\eta_p^2=0.142$) and applied MLM category (main effect, $p<0.001$, $\eta_p^2=0.084$), and also R^2 values are significantly affected by the calibration speed mode (main effect, $p<0.001$, $\eta_p^2=0.098$) and applied MLM category (main effect, $p<0.001$, $\eta_p^2=0.095$). The pairwise comparisons show that across all prediction scenarios with every speed mode calibration, the proposed sEMG-US imaging-derived MLM could significantly reduce the $BW-RMSE$ values by 14.49% ($p=0.029$, $d=-0.348$) and 23.84% ($p=0.004$, $d=-0.689$), significantly reduce the $N-RMSE$ values by 14.58% ($p=0.012$, $d=-0.389$) and 23.69% ($p=0.006$, $d=-0.707$), and increase the R^2 values by 3.71% ($p=0.063$, $d=0.371$) and 6.96% ($p<0.001$, $d=0.725$) compared to sEMG-driven and US imaging-driven MLMs, respectively. Furthermore, the pairwise comparisons also show that across all prediction scenarios with every MLM category, the inter-speed mode calibration could reduce the $BW-RMSE$ values by 38.74% ($p<0.001$, $d=-0.922$), 18.86% ($p=0.184$, $d=-0.390$), 8.87% ($p=0.926$, $d=-0.237$), 9.84% ($p=0.885$,

Table I: Correlation coefficients (mean±SD) between each neuromuscular feature and the net PF moment across five participants at each walking speed.

		Neuromuscular features			
		LGS sEMG	SOL sEMG	LGS MT	SOL MT
Speed [m/s]	0.5	0.886 (0.019)	0.876 (0.086)	0.857 (0.052)	0.867 (0.053)
	0.75	0.890 (0.058)	0.905 (0.054)	0.842 (0.024)	0.865 (0.032)
	1.0	0.892 (0.066)	0.896 (0.056)	0.883 (0.063)	0.892 (0.056)
	1.25	0.835 (0.096)	0.857 (0.076)	0.840 (0.034)	0.833 (0.033)
	1.5	0.801 (0.124)	0.785 (0.081)	0.847 (0.018)	0.844 (0.022)

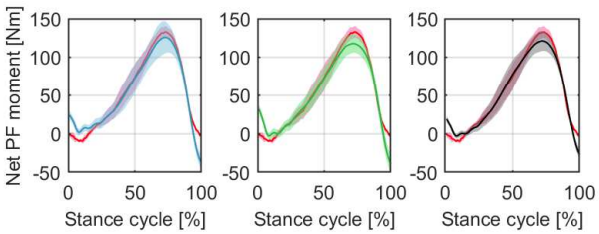

(a) With the single-speed mode calibrated MLMs

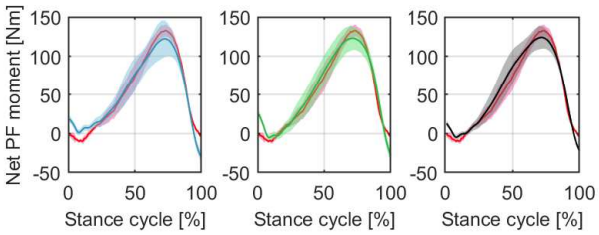

(b) With the inter-speed mode calibrated MLMs

Figure 3: Net PF moment prediction comparison by using sEMG-/US imaging-/sEMG-US imaging-driven MLMs at 1.0 m/s walking speed on Sub05. The red, blue, green, and black lines with shadowed areas represent the mean and SD of the net PF moment from ID calculation, sEMG-driven MLM prediction, US imaging-driven MLM prediction, and sEMG-US imaging-driven MLM prediction, respectively.

$d = -0.299$), and 26.57% ($p = 0.004$, $d = -0.836$), reduce the $N - RMSE$ values by 35.73% ($p < 0.001$, $d = -1.002$), 17.20% ($p = 0.201$, $d = -0.403$), 9.11% ($p = 0.881$, $d = -0.254$), 11.44% ($p = 0.715$, $d = -0.326$), and 28.08% ($p < 0.001$, $d = -0.817$), and increase the R^2 values by 16.76% ($p < 0.001$, $d = 0.810$), 5.33% ($p = 0.307$, $d = 0.342$), 0.04% ($p = 0.996$, $d = 0.004$), 0.31% ($p = 0.921$, $d = 0.033$), and 6.51% ($p = 0.127$, $d = 0.487$) compared to single-speed mode calibration at 0.5 m/s, 0.75 m/s, 1.0 m/s, 1.25 m/s, and 1.5 m/s, respectively.

This study for the first time investigated the continuous ankle joint net PF moment prediction during the walking stance phase, based on a dual-modal approach with the consideration of combining sEMG- and US imaging-derived neuromuscular features. The results from five young able-bodied participants indicated that there was superior net PF moment prediction performance by using the sEMG-US imaging-driven MLM compared to sEMG-driven and US imaging-driven MLMs, validating our hypothesis. The MLM calibration and prediction in this work simplified the sophisticated HNM calibration and prediction [9], [19], which depend on a plethora of subjective physiological variables. Compared to the physiology-based personalized HNM, machine learning approaches, like MLM in this work, do not require specific physiological meanings of the input variables, and their training procedures are relatively simple and straightforward. The evaluation of the MLMs' calibration and prediction performance was based on three criteria: $BW - RMSE$, $N - RMSE$, and R^2. In general, as reported in [25], the results were considered excellent if the $N - RMSE$ values were smaller than 15%. The results in Fig. 4 show the mean $N - RMSE$ values are all less than 11.5% regardless of the calibration speed modes (single-speed or inter-speed mode) and applied MLM categories throughout those five walking speeds scenarios, which validates the prediction results are all excellent. As a preliminary study of the sEMG-US imaging-driven MLM for dynamic walking on a treadmill with multiple speeds, the results are promising and can help overcome the challenges of joint motion intent detection in volitional control of assistive devices. This work has extended the preliminary results of voluntary isometric ankle PF experiments [22] to dynamic walking experiments on able-bodied participants. Further experiments on patients with impaired plantar flexors are needed to verify the practicability of the proposed sEMG-US imaging-driven MLM for ankle joint net PF moment prediction.

IV. Conclusion

This paper investigated an sEMG-US imaging-driven MLM to predict ankle joint net PF moment during the stance phase at multiple walking speeds. The processed sEMG and US imaging-derived MT signals from both LGS and SOL muscles were used to calibrate single-speed and inter-speed MLMs. The results obtained from five able-bodied participants showed that on average the net PF moment prediction $RMSE$ was statistically significantly reduced when using the sEMG-US imaging-driven MLM, compared to sEMG-driven and US imaging-driven MLMs across all participants and walking speeds. The results also showed that the calibrated MLMs with inter-speed mode provided more robust net PF moment prediction at different speed scenarios than calibrated MLMs with single-speed modes. The improved net PF moment prediction due to the use of sEMG and US imaging's combination could potentially lead to improvements in human-robot-interaction and volitional control of assistive devices with more advanced and intelligent algorithms, such as AAN control with adaptive impedance during the walking stance phase.

References

[1] P. H. Tzu-wei, K. A. Shorter, P. G. Adamczyk, and A. D. Kuo, "Mechanical and energetic consequences of reduced ankle plantarflexion in human walking," *J. Exp. Biol.*, vol. 218, no. 22, pp. 3541–3550, 2015.

[2] K. Z. Takahashi, M. D. Lewek, and G. S. Sawicki, "A neuromechanics-based powered ankle exoskeleton to assist walking post-stroke: a feasibility study," *J. NeuroEngineering Rehabil.*, vol. 12, no. 1, p. 23, 2015.

[3] F. Tamburella, N. Tagliamonte, I. Pisotta, M. Masciullo, M. Arquilla, E. Van Asseldonk, H. van Der Kooij, A. Wu, F. Dzeladini, A. Ijspeert *et al.*, "Neuromuscular controller embedded in a powered ankle exoskeleton: Effects on gait, clinical features and subjective perspective of incomplete spinal cord injured subjects," *IEEE Trans. Neural Syst. Rehabil. Eng.*, vol. 28, no. 5, pp. 1157–1167, 2020.

[4] B. Quinlivan, S. Lee, P. Malcolm, D. Rossi, M. Grimmer, C. Siviy, N. Karavas, D. Wagner, A. Asbeck, I. Galiana *et al.*, "Assistance magnitude versus metabolic cost reductions for a tethered multiarticular soft exosuit," *Sci. Robot.*, vol. 2, no. 2, p. eaah4416, 2017.

[5] A. Selfslagh, S. Shokur, D. S. Campos, A. R. Donati, S. Almeida, S. Y. Yamauti, D. B. Coelho, M. Bouri, and M. A. Nicolelis, "Non-invasive, brain-controlled functional electrical stimulation for locomotion rehabilitation in individuals with paraplegia," *Sci. Rep.*, vol. 9, no. 1, pp. 1–17, 2019.

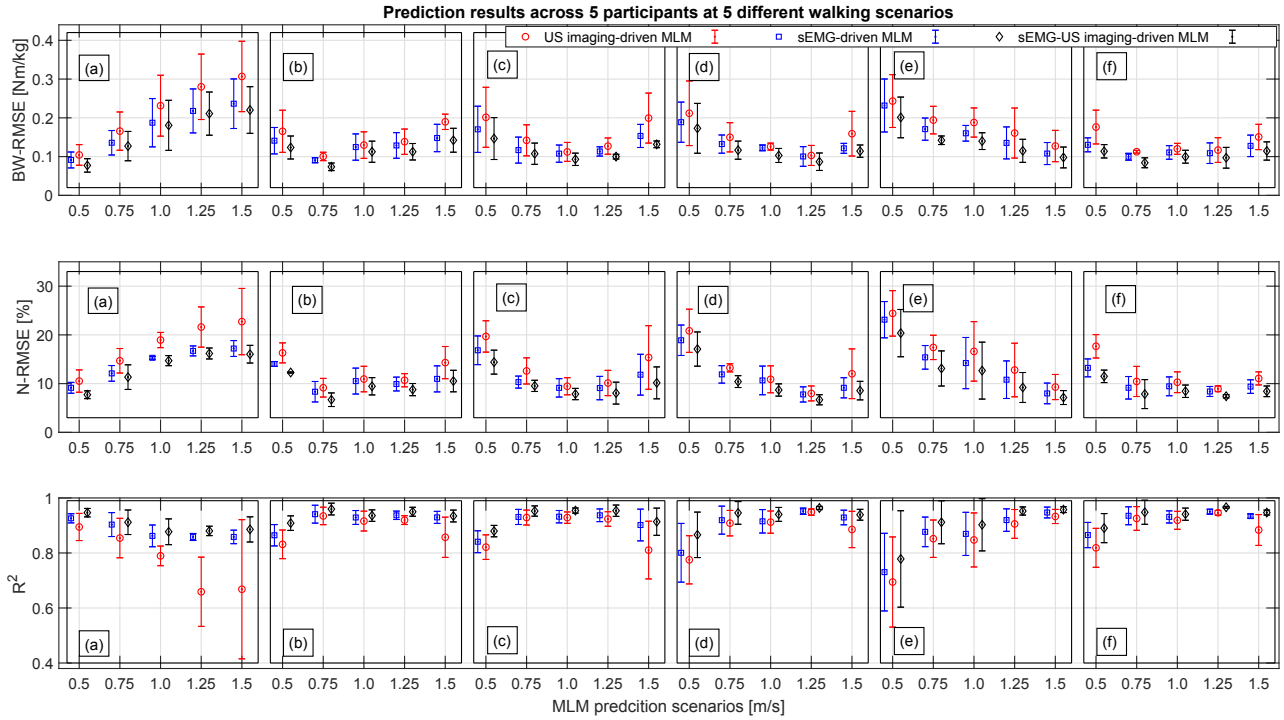

Figure 4: $BW-RMSE$, $N-RMSE$, and R^2 values of the ankle joint net PF moment prediction across 5 participants by applying the calibrated MLMs with different speed modes. Column subplots from (a) to (e) represent the applied calibrated MLMs at single-speed mode of 0.5 m/s, 0.75 m/s, 1.0 m/s, 1.25 m/s, 1.5 m/s, and the inter-speed mode.

[6] S. Hussain, P. K. Jamwal, M. H. Ghayesh, and S. Q. Xie, "Assist-as-needed control of an intrinsically compliant robotic gait training orthosis," *IEEE Trans. Ind. Electron.*, vol. 64, no. 2, pp. 1675–1685, 2016.

[7] D. Zanotto, Y. Akiyama, P. Stegall, and S. K. Agrawal, "Knee Joint Misalignment in Exoskeletons for the Lower Extremities: Effects on User's Gait," *IEEE Trans. Robot.*, vol. 31, no. 4, pp. 978–987, 2015.

[8] M. Sartori, D. Farina, and D. G. Lloyd, "Hybrid neuromusculoskeletal modeling to best track joint moments using a balance between muscle excitations derived from electromyograms and optimization," *J. Biomech.*, vol. 47, no. 15, pp. 3613–3621, 2014.

[9] Q. Zhang, K. Kim, and N. Sharma, "Prediction of Ankle Dorsiflexion Moment by Combined Ultrasound Sonography and Electromyography," *IEEE Trans. Neural Syst. Rehabil. Eng.*, vol. 28, no. 1, pp. 318–327, 2020.

[10] J. Han, Q. Ding, A. Xiong, and X. Zhao, "A state-space emg model for the estimation of continuous joint movements," *IEEE Trans. Ind. Electron.*, vol. 62, no. 7, pp. 4267–4275, 2015.

[11] Q. Zhang, A. Iyer, Z. Sun, K. Kim, and N. Sharma, "A Dual-modal Approach Using Electromyography and Sonomyography Improves Prediction of Dynamic Ankle Dorsiflexion Motion," *IEEE Trans. Neural Syst. Rehabil. Eng.*, Under review, 2021.

[12] D. L. Crouch, L. Pan, W. Filer, J. W. Stallings, and H. Huang, "Comparing Surface and Intramuscular Electromyography for Simultaneous and Proportional Control Based on a Musculoskeletal Model: A Pilot Study," *IEEE Trans. Neural Syst. Rehabil. Eng.*, vol. 26, no. 9, pp. 1735–1744, 2018.

[13] E. M. Strasser, T. Draskovits, M. Praschak, M. Quittan, and A. Graf, "Association between ultrasound measurements of muscle thickness, pennation angle, echogenicity and skeletal muscle strength in the elderly," *Age*, vol. 35, no. 6, pp. 2377–2388, 2013.

[14] A. Arampatzis, K. Karamanidis, S. Stafilidis, G. Morey-Klapsing, G. DeMonte, and G.-P. Brüggemann, "Effect of different ankle-and knee-joint positions on gastrocnemius medialis fascicle length and emg activity during isometric plantar flexion," *J. Biomech.*, vol. 39, no. 10, pp. 1891–1902, 2006.

[15] Q. Zhang, A. Iyer, K. Kim, and N. Sharma, "Evaluation of non-invasive ankle joint effort prediction methods for use in neurorehabilitation using electromyography and ultrasound imaging," *IEEE Trans. Biomed. Eng.*, vol. 68, no. 3, pp. 1044–1055, 2021.

[16] D. L. Damiano, L. A. Prosser, L. A. Curatalo, and K. E. Alter, "Muscle plasticity and ankle control after repetitive use of a functional electrical stimulation device for foot drop in cerebral palsy," *Neurorehabil. Neural Repair*, vol. 27, no. 3, pp. 200–207, 2013.

[17] E. Hodson-Tole and A. Lai, "Ultrasound-derived changes in thickness of human ankle plantar flexor muscles during walking and running are not homogeneous along the muscle mid-belly region," *Sci. Rep.*, vol. 9, no. 1, pp. 1–11, 2019.

[18] J.-Y. Guo, Y.-P. Zheng, H.-B. Xie, and X. Chen, "Continuous monitoring of electromyography (EMG), mechanomyography (MMG), sonomyography (SMG) and torque output during ramp and step isometric contractions," *Med. Eng. Phys.*, vol. 32, no. 9, pp. 1032–1042, 2010.

[19] T. J. M. Dick, A. A. Biewener, and J. M. Wakeling, "Comparison of human gastrocnemius forces predicted by Hill-type muscle models and estimated from ultrasound images," *J. Exp. Biol.*, vol. 220, no. 9, pp. 1643–1653, 2017.

[20] M. H. Jahanandish, N. P. Fey, and K. Hoyt, "Lower-Limb Motion Estimation Using Ultrasound Imaging: A Framework For Assistive Device Control," *IEEE J. Biomed. Health Inform.*, pp. 1–10, 2019.

[21] Y. Fang, N. Hettiarachchi, D. Zhou, and H. Liu, "Multi-modal sensing techniques for interfacing hand prostheses: A review," *IEEE Sensors Journal*, vol. 15, no. 11, pp. 6065–6076, 2015.

[22] Q. Zhang, A. Iyer, K. Kim, and N. Sharma, "Volitional contractility assessment of plantar flexors by using non-invasive neuromuscular measurements," in *2020 8th IEEE RAS/EMBS International Conference for Biomedical Robotics and Biomechatronics (BioRob)*. IEEE, pp. 515–520.

[23] D. A. Winter, *Biomechanics and motor control of human movement*. John Wiley & Sons, 2009.

[24] D. J. Farris and G. A. Lichtwark, "UltraTrack: Software for semi-automated tracking of muscle fascicles in sequences of B-mode ultrasound images," *Comput. Methods Programs Biomed.*, vol. 128, pp. 111–118, 2016.

[25] M. M. Liu, W. Herzog, and H. H. Savelberg, "Dynamic muscle force predictions from EMG: an artificial neural network approach," *J. Electromyogr. Kinesiol.*, vol. 9, no. 6, pp. 391–400, 1999.